J Prosthodont Res. 2022; **(**): ****–****

OPEN ACCESS JPR osthodontic esearch

Journal of Prosthodontic Research

Original article

Optimization of blood and protein flow around superhydrophilic implant surfaces by promoting contact hemodynamics

Hiroaki Kitajima [a,b], Makoto Hirota [a,b,c], Kohei Osawa [b], Toshinori Iwai [b], Juri Saruta [a,d], Kenji Mitsudo [b], Takahiro Ogawa [a,*]

[a] Weintraub Center for Reconstructive Biotechnology, Division of Regenerative and Reconstructive Sciences, UCLA School of Dentistry

[b] Department of Oral and Maxillofacial Surgery, Graduate School of Medicine, Yokohama City University, Yokohama, Japan

[c] Department of Oral and Maxillofacial Surgery/Orthodontics, Yokohama City University Medical Center, Yokohama, Japan

[d] Department of Education Planning, School of Dentistry, Kanagawa Dental University, Yokosuka, Japan

Abstract

Purpose: We examined blood and protein dynamics potentially influenced by implant threads and hydrophilic/hydrophobic states of implant surfaces.

Methods: A computational fluid dynamics model was created for a screw-shaped implant with a water contact angle of 70° (hydrophobic surface) and 0° (superhydrophilic surface). Movements and density of blood and fibrinogen as a representative wound healing protein were visualized and quantified during constant blood inflow.

Results: Blood plasma did not occupy 40–50% of the implant interface or the inside of threads around hydrophobic implants, whereas such blood voids were nearly completely eliminated around superhydrophilic implants. Whole blood field vectors were disorganized and random within hydrophobic threads but formed vortex nodes surrounded by stable blood streams along the superhydrophilic implant surface. The averaged vector within threads was away from the implant surface for the hydrophobic implant and towards the implant surface for the superhydrophilic implant. Rapid and massive whole blood influx into the thread zone was only seen for the superhydrophilic implant, whereas a line of conflicting vectors formed at the entrance of the thread area of the hydrophobic implant to prevent blood influx. The fibrinogen density was up to 20-times greater at the superhydrophilic implant interface than the hydrophobic one. Fibrinogen density was higher at the interface than outside the threads only for the superhydrophilic implant.

Conclusions: Implant threads and surface hydrophilicity have profound effects on vector and distribution of blood and proteins. Critically, implant threads formed significant biological voids at the interface that were negated by superhydrophilicity-induced contact hemodynamics.

Keywords: Computational fluid dynamics (CFD), Bone-implant integration, Osseointegration, UV activation/photofunctionalization, Titanium implant

Received 30 August 2022, Accepted 5 December 2022, Available online 22 December 2022

1. Introduction

Despite the widespread use of metallic implants in orthopedic surgery and dentistry, gaps remain in our understanding of the biology of bone-implant integration, or osseointegration. Fundamental questions exist about osseointegration, including whether bone-implant integration differs from natural bone healing, why bone formation initiates at the implant interface and concentrically distant from the implant surface, and why bone remodeling and resorption vary in different regions around the implant[1–3]. Although the design of implant screw threads has been refined from a mechanical perspective for better initial implant stability, the biological impact of thread design has not been explored. Various implant surfaces have been developed to accelerate and enhance bone-implant integration, but the biological mechanisms underpinning these improvements have yet to be fully investigated[4–26].

Ultraviolet (UV) light has recently been used to favorably modify implant surfaces[2,3,27–50]. For example, titanium surfaces, regardless of their surface texture, are hydrophobic (H_2O contact angle ≥60°), and treating these surfaces with UV light converts them to a superhydrophilic state with a contact angle of ≤5° or 0° for the majority of currently used titanium surfaces[30,51–63]. This UV-induced hydrophilic conversion also occurs with other implant materials including titanium alloy, chromium-cobalt alloy, and zirconia[29,38,39,41,42,44,45,47,64–68]. These superhydrophilic implant surfaces promote cell attachment and increase the speed and percentage of bone coverage around the implants[2,3,9,30,32,34,69–72]. Osteogenesis around superhydrophilic implants is concentrated at

DOI: https://doi.org/10.2186/jpr.JPR_D_22_00225

***Corresponding author:** Takahiro Ogawa, Weintraub Center for Reconstructive Biotechnology, Division of Advanced Prosthodontics, UCLA School of Dentistry, 10833 Le Conte Avenue, B3-087, Box951668, Los Angeles, CA 90095-1668.

E-mail address: togawa@dentistry.ucla.edu

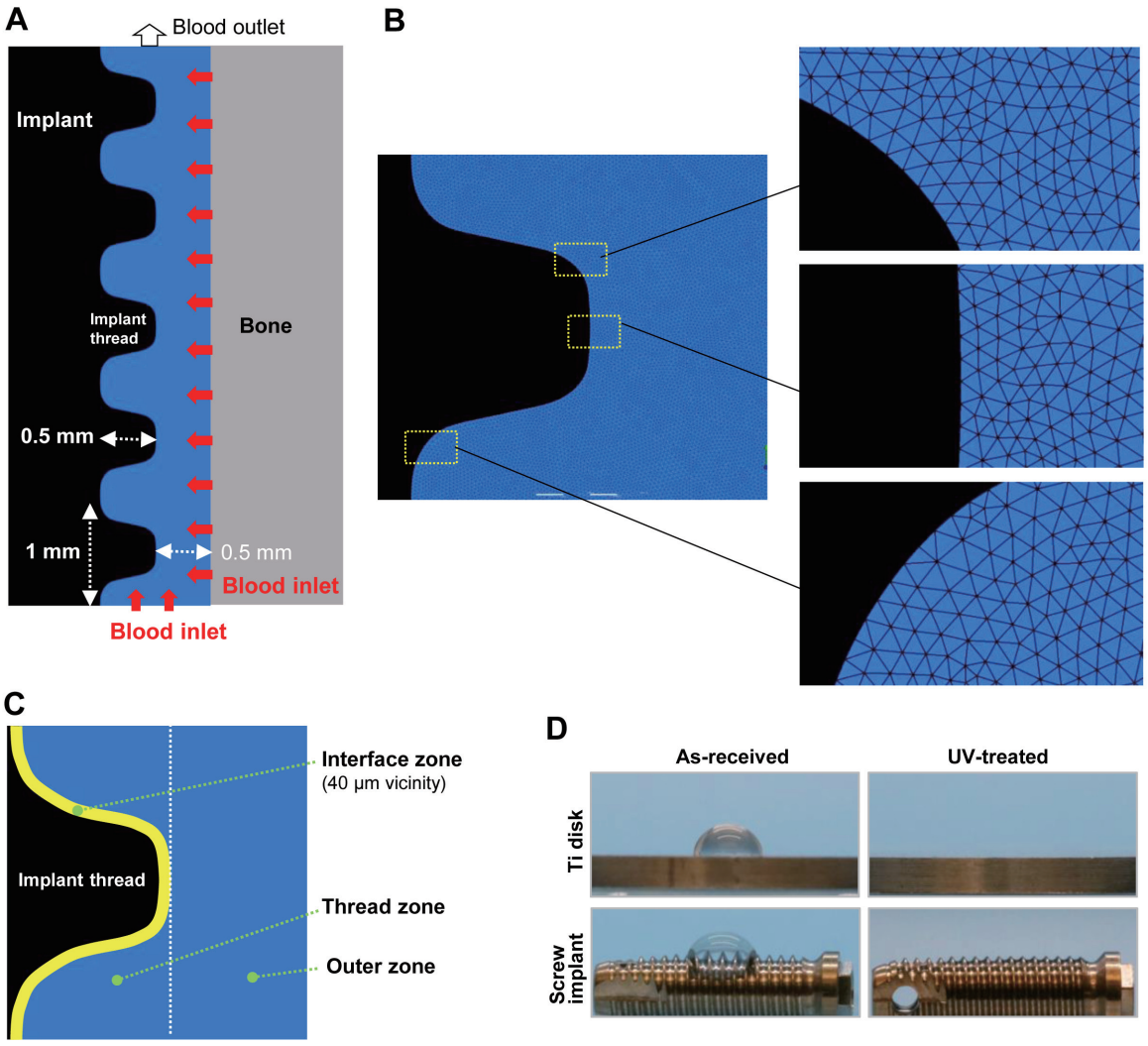

Fig. 1. Computational fluid dynamics (CFD) model of a screw-shaped implant to simulate the interaction between blood and implant morphology and surface hydrophilicity. (A) Dimensions of an implant and surrounding local environment in the model, with boundary conditions. (B) Meshing to generate triangular cells. (C) The definition of the three different zones to analyze blood and protein dynamics. (D) Hydrophobicity or hydrophilicity measurements of implant materials. Side-view photographs of 10 μL of ddH_2O placed on titanium disks and screw-shaped dental implants. As-received and UV-treated titanium materials were tested.

the implant interface, with rapid bone remodeling in areas slightly distant from the implant surface[3,30]. However, how the superhydrophilic implant surface controls these biological processes is currently unknown, although it is speculated that the superhydrophilic surface prevents air bubble formation at the implant interface, thereby ensuring blood access[41,49,51,59,73].

We hypothesized that implant morphology and surface hydrophobicity or hydrophilicity alter blood flow and coordinated protein movement. However, examining these biological events around implants *in vivo* is extremely difficult. We therefore created an *in silico* implant model using computational fluid dynamics (CFD) and analyzed the concentration, vectors, and other fluid behaviors of blood and fibrinogen around hydrophobic and superhydrophilic implants, with fibrinogen chosen as a model protein as it plays a significant role in bone healing.

2. Materials and methods

2.1. Hydrophobic-to-superhydrophilic conversion of implant surfaces

Hydrophobicity or hydrophilicity was quantified by measuring the contact angle of 10 μL of ddH_2O placed on 20 mm diameter grade 4 titanium disks prepared by machining and commercially available dental implants (Brånemark System, diameter, 3.75 mm and length 13 mm; Nobel Biocare, Yorba Linda, CA). As-received control titanium and UV-treated titanium were tested. Ultraviolet treatment was conducted by irradiating a combination of UVA and UVC for 20 min.

2.2. Computational fluid dynamics implant model

A screw-shaped geometric model was created using ANSYS Design Modeler (2019 R1; ANSYS Inc., Canonsburg, PA) to mimic the peri-implant local environment (**Fig. 1A**). The model consisted of

five threads and four boundaries: blood inlet, bone, blood outlet, and implant surface. The model was subjected to mesh generation using ANSYS meshing, and the domain was divided into 1,498,162 triangular cells (**Fig. 1B**). The fluid field was divided into three zones: the interface, thread, and outer zones (**Fig. 1C**), where the interface zone was defined as an area within 40 μm of the implant surface and the thread zone as the area surrounded by the implant threads. The outer zone was the area outside the implant threads or the remaining fluid field.

2.3. Analytical method

The volumes of fraction (VOF) and species transport models in ANSYS Fluent (2019 R1; ANSYS Inc.) were utilized to analyze the flow of blood plasma, red blood cells (RBCs), fibrinogen, and whole blood, where the fibrinogen is a subset of blood plasma and the blood plasma, RBCs, and fibrinogen are the subsets of whole blood. All equations used in the analysis are defined and described in the ANSYS Theory Guide and User's Guide[74,75].

2.3.1. Volumes of fraction model

The ANSYS Fluent VOF model can track the free interface between two fluid phases by solving a continuity equation for the VOF. Blood plasma and RBCs were set as primary and secondary phases, respectively. The interfacial tension between the blood plasma and RBCs was set as 0.021 N/m as established by Mottaghy and Hahn[76]. Red blood cells were considered a continuum because the fluid zone was larger than the diameter of an RBC (<7 μm).

2.3.2. Species transport model

The concentration (mass fraction) of fibrinogen in blood plasma was tracked using a species transport equation:

$$\frac{\partial}{\partial t}\left(\rho_m Y_i\right)+\nabla\cdot\left(\rho_m \vec{v} Y_i\right)=-\nabla\vec{J_i} \quad \text{(1) [74]}$$

where ρ_m is the density of the mixture of blood plasma and fibrinogen, Y_i is the local mass fraction of each species, and subscript i is species number set to 0 and 1 for fibrinogen and blood plasma, respectively. Equation (1) was solved to calculate the mass fraction of fibrinogen (Y_0). The local mass fraction of blood plasma (Y_1) was calculated as 1-Y_0, because the sum of the local mass fractions is 1. $\vec{J_i}$ is the diffusion flux of species i. Fick's law was used to model mass diffusion owing to concentration gradients, in which $\vec{J_i}$ can be written as

$$\vec{J_i}=-\rho_m D_{i,m} Y_i \quad \text{(2) [74]}$$

where $D_{i,m}$ is the diffusion coefficient for species i in the mixture. The diffusion coefficient between fibrinogen and blood has not been previously measured. Therefore, the diffusion coefficient between fibrinogen and water (0.23×10^{-10} m^2/s) was used for $D_{0,m}$, according to Nauman *et al.*[77]. It was assumed that no chemical reaction happens between species and the transfer of temperature was considered negligible.

2.4. Fluid properties

The density and viscosity of RBCs were defined as constants of 1125 kg/m^3[78] and 0.0050 Pa·s[79], respectively. The volume-weighted mixing law in ANSYS Fluent was applied as the density of the mixture of blood plasma and fibrinogen (ρ_m), which enabled the values to be calculated according to Y_i. With this model, the density can be written as

$$\rho_m=\frac{1}{\sum_i \frac{Y_i}{\rho_i}} \quad \textbf{(3)} \text{ [75]}$$

where the densities of fibrinogen (ρ_0) and blood plasma (not including fibrinogen, ρ_1) were set to 1400[80] and 1025 kg/m^3[78], respectively. The viscosity of the mixture (μ_m) was calculated according to the function of the concentration of fibrinogen in blood plasma based on a previous study[81]:

$$\mu_m=\begin{cases}\left(1.16C+0.53\right)\times 1\times 10^{-3} & \text{if } 0\le C<0.40\\ \left(0.37C+0.85\right)\times 1\times 10^{-3} & \text{if } 0.40\le C<1.00\\ \left(0.19C^2+1.03\right)\times 1\times 10^{-3} & \text{if } 1.00\le C\end{cases} \quad \textbf{(4)} \text{ [81]}$$

where C is the concentration of fibrinogen (g/100 mL) in blood plasma.

2.5. Numerical conditions

The boundary condition in this study assumes blood flow from capillaries distributed in the alveolar bone. Studies that have measured the velocity of RBCs in the capillaries show that their values range from 1.0 to 4.0 mm/s[82]. Therefore, the velocity at the blood inlet and in alveolar bone was set to 0.001 m/s. For the outflow boundary condition, a free stream boundary condition was used. The contact angle between blood plasma and the implant surface was set to 70° and 0° based on the results from the above-mentioned contact angle measurements (**Fig. 1D**). A normal adult human hematocrit (45%) was used as the VOF value at the blood flow inlet and alveolar bone; therefore, the VOF for blood plasma was 55%. The mass fraction of fibrinogen (Y_0) at the blood flow inlet and alveolar bone was 0.29% and was obtained by dividing the normal adult human fibrinogen concentration (300 mg/dL = 3 kg/m^3) by the density of blood serum (1024 kg/m^3)[83]. Time step size and the number of steps were set to 0.0001 s and 30,000, respectively. The pressure-based solver in ANSYS Fluent was used as it was necessary for VOF modeling. The calculation at each time step was considered to have reached convergence when the rate of change in the mass flow of fibrinogen (kg/s) reached below 0.01. A double precision solver was used. Pressure-velocity coupling was achieved using the coupled scheme. As the Reynold's number was sufficiently lower than the value at which the flow field transitions into a turbulent flow (i.e., 2800), the flow field within the fluid zone was considered laminar. The analysis was conducted on a single computer running Microsoft Windows 10 Professional (Microsoft Corp., Redmond, WA). The data were exported into CFD-POST (2019 R1; ANSYS Inc.) to visualize the valuables in the fluid zone.

2.6. Vorticity of fluid field

Vorticity was also calculated to further capture the characteristics of the flow field. Vorticity represents the local spinning motion of a continuum and is expressed by the following standard equation.

$$\hat{\imath} = \frac{\partial v}{\partial x} - \frac{\partial u}{\partial y} \quad (5)$$

where ξ is vorticity (s^{-1}) and v and u are the velocity components in the fluid zone parallel and vertical to the implant body, respectively. Under the definition written above, a flow field with a positive vorticity indicates the existence of a counterclockwise vortex.

3. Results

3.1. Confirmation of the hydrophilic conversion of titanium after UV treatment

We first verified the conversion of regular titanium surfaces from a hydrophobic state to a superhydrophilic state after UV light treatment. A 10 μL ddH_2O drop placed on a machined grade 4 titanium disk did not spread and remained hemispherical with a contact angle of 70.2° (top panels in **Fig. 1D**), indicating a hydrophobic surface. In contrast, a ddH_2O drop placed on a UV-treated titanium disk spread immediately over the surface and had a contact angle of 0.0°, indicating a superhydrophilic surface. Hydrophobicity or hydrophilicity was also tested on screw-shaped dental implants (bottom panels in **Fig. 1D**), which confirmed hydrophobic and superhydrophilic surfaces before and after UV treatment, respectively. These results confirmed that UV light induces hydrophobic-to-superhydrophilic conversion, even on identical titanium surfaces, and validated the hydrophobicity and hydrophilicity parameters of 70.0° and 0.0° used in the CFD implant model.

3.2. Blood flow visualization by density mapping around hydrophobic and superhydrophilic implants

To describe the overall qualitative blood flow around implants, we first color-mapped the blood plasma density around implants with either hydrophobic (contact angle 70°) or superhydrophilic (contact angle 0°) surfaces from the start of blood flow up to 3 seconds. Blood entered at the apex of the implant and the axial wall of the surrounding bone and exited upwards as shown in **Figures 1A and 2**. As shown in color mappings at different time points (**Fig. 2**), there were clear differences in flow behavior between hydrophobic and superhydrophilic implants. Around the hydrophobic implant, some blood plasma infiltrated the thread zone 1 second after the start of blood flow. However, blood plasma did not completely fill the thread zone of the hydrophobic implant, leaving a substantial part of the implant interface free from blood plasma throughout the period of analysis. The blood plasma voids were randomly localized and shaped, although most stemmed from the implant interface and extended into the outer zone. Part of the hydrophobic implant interface and thread zone, even when filled with blood plasma, showed a low concentration of blood plasma (white arrowheads in the 3-second density mapping).

In contrast, nearly the entire implant interface and thread zone of the superhydrophilic implant were filled with blood plasma throughout the analysis period (**Fig. 2**). Density mapping indicated that, compared with the outer zone, the interface and thread zones were highly concentrated with blood and contained nearly no voids. The increased density at the interface and thread was more even for the superhydrophilic implant than for the hydrophobic implant. Blood plasma voids appeared exclusively in the outer zone of the superhydrophilic implant and were apparently smaller than those around the hydrophobic implant.

Several magnified mappings are presented to show a characteristic blood plasma density profile (**Figs. 2a-d**). The edge of the blood consisted of a thin layer of the lowest blood density, as depicted by blue lines facing all voids (a-d). However, when the blood faced an implant surface (a and b), no such layer was found at the blood-implant interface. As a result, all implant interfaces, if covered with blood plasma, received a good density of blood, as typically seen on the superhydrophilic surface (panels c and d). A short, slow motion video was created based on the sequential blood plasma density mapping images to clearly visualize the blood fluid dynamics (https://indd.adobe.com/view/c046e3b2-b3c9-443f-a2f1-c640519346d9).

3.3. Quantitative assessment of blood plasma voids around hydrophobic and superhydrophilic implants

We next proceeded to quantify the blood dynamics, starting with blood plasma void occurrence (**Fig. 3**). The white areas in **Figure 2**, representing the absence of blood plasma or the localization of RBCs, were defined as voids, because of the lack of nutritious fluid and protein. Void occurrence in the interface zone was defined as the percentage of the interfacial length with no juxtaposing blood plasma relative to the entire interfacial length, and the void occurrence in the thread and outer zones was defined as the percentage area with no blood plasma relative to the entire area of each zone. The hydrophobic implant interface showed a void greater than 15% during the initial 1 second, and the void occurrence increased rapidly with time, with nearly 50% of the interface lacking blood at 3 seconds (**Fig. 3A**). In contrast, the void occurrence remained very low or even absent at the superhydrophilic interface throughout the period of analysis. The result was similar in the thread zone, with void occurrence worsening over time around the hydrophobic implant, reaching close to 40% at 3 seconds (**Fig. 3B**). The thread zone void was consistently low around the superhydrophilic implant with no significant time-dependency, and reached 0 at 3 seconds. The void occurrence in the outer zone was not time-dependent for both implants and was significantly lower around the superhydrophilic implant than the hydrophobic implant (**Fig. 3C**). Of note, voids were generated more often in the interface zone than in the outer zone for the hydrophobic implant, whereas this was reversed for the superhydrophilic implant, which had more voids in the outer zone.

3.4. Direction and velocity of whole blood flow around hydrophobic and superhydrophilic implants

We next analyzed vector field formation during blood flow. Field vectors indicate both direction and magnitude of the center of each cell in the CFD grid and allow the interpretation of both the direction and velocity of whole blood flow. **Figures 4A-C** show the average values of the horizontal component of the vectors and **Figures 4D-F** the average value of the vertical component.

The average vector direction was away from the implant in the interface zone of the hydrophobic implant, with its velocity

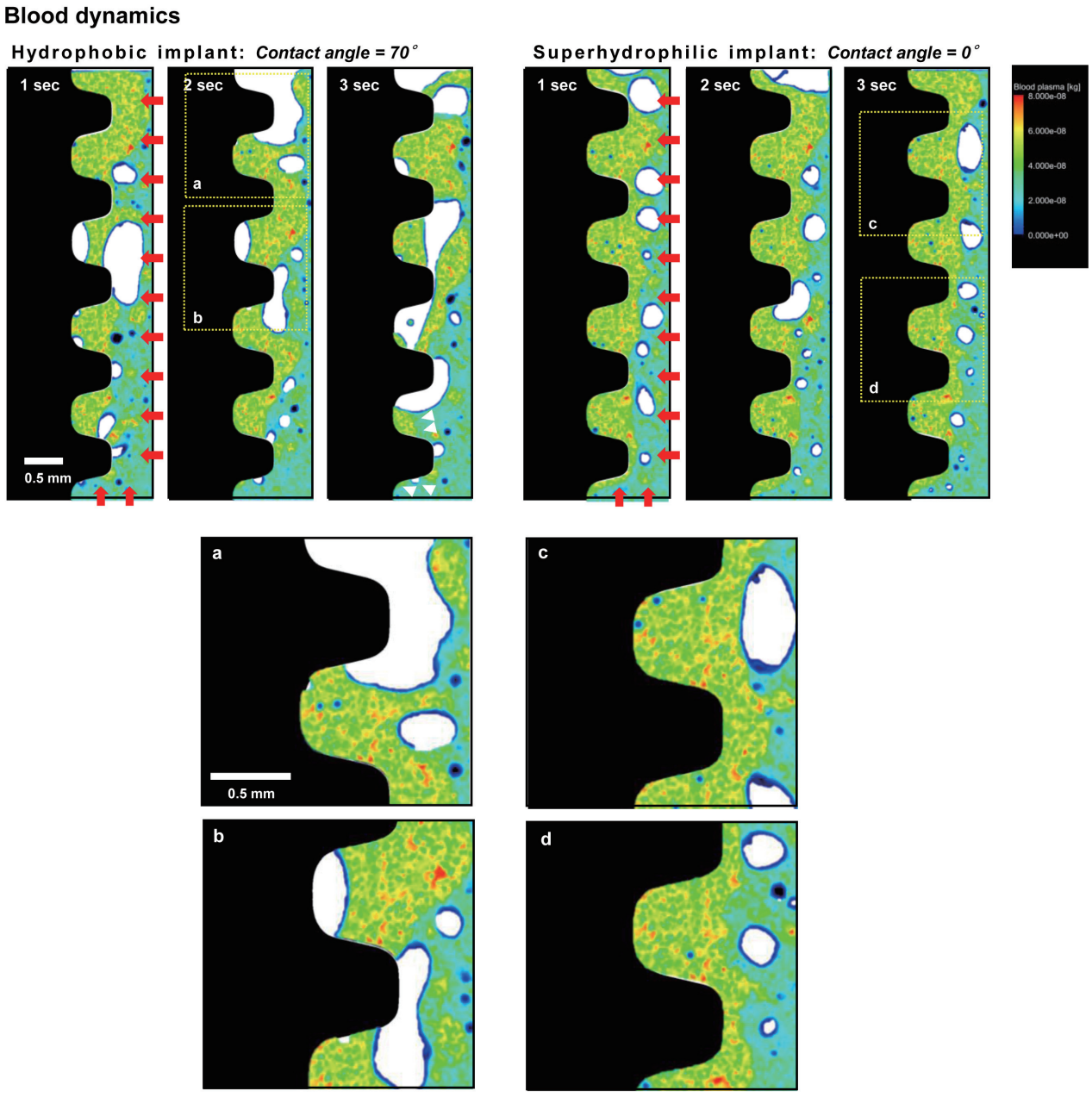

Fig. 2. Blood dynamics visualized by color-mapping the blood plasma density and comparing hydrophobic and superhydrophilic implants with their contact angles of 70° and 0°, respectively. Images from three different time points are presented. The blood inlet is indicated by red arrows. Magnified images (a-d) are also provided for the dotted squares a-d.

increasing with time (**Fig. 4A**). Conversely, the average vector at the superhydrophilic interface was directed towards the implant and was substantially faster than around the hydrophobic implant and increased with time. The trend was similar in the thread zone; i.e., the averaged vector direction was opposite in the different implants (**Fig. 4B**). The average vector was oriented towards the implant in the outer zone for both implants (**Fig. 4C**). A comparison of the different zones indicated that the horizontal blood velocity was greater in the thread zone than in the outer zone only for the superhydrophilic implant.

The average blood vector was upward in all zones regardless of the hydrophobic or superhydrophilic state (**Figs. 4D-F**). The vertical component of the vectors was greater for the superhydrophilic implant than for the hydrophobic implant in the interface and thread zones. The upward blood velocity in the thread zone was remarkably slower than in the outer zone for both implants; 1/8 to 1/6 around the hydrophobic implants and 1/4 to 1/3 around the superhydrophilic implants. Based on these averaged vectors, blood dynamics are summarized in **Figure 5**, in which yellow arrows depict the overall direction and speed of whole blood flow for hydrophobic and superhydrophilic implants.

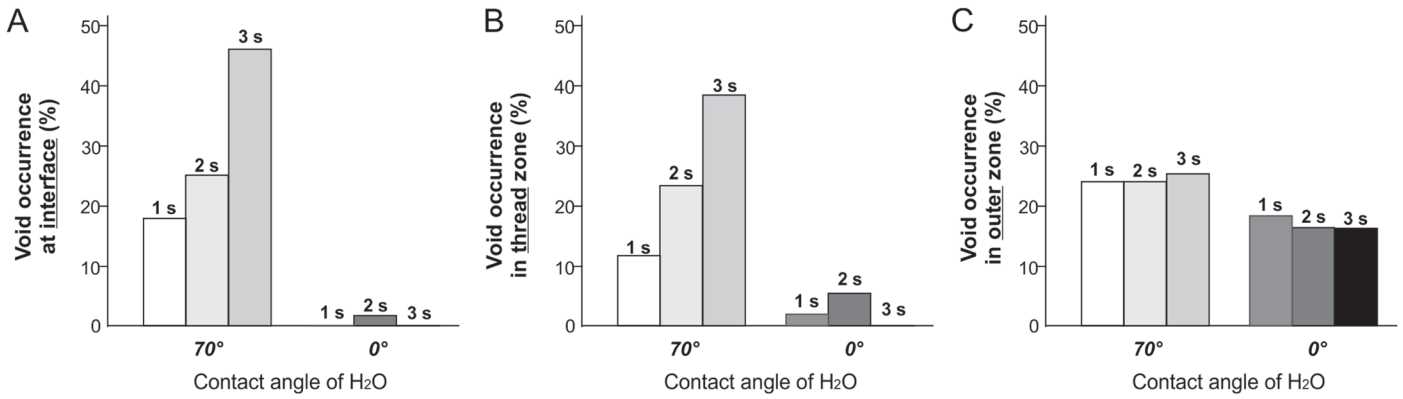

Fig. 3. Quantitative assessment of the occurrence of blood plasma voids during blood flow. The percentage of void areas relative to the domain was calculated for the interface, thread, and outer zones and presented to compare hydrophobic (70°) and superhydrophilic (0°) implants.

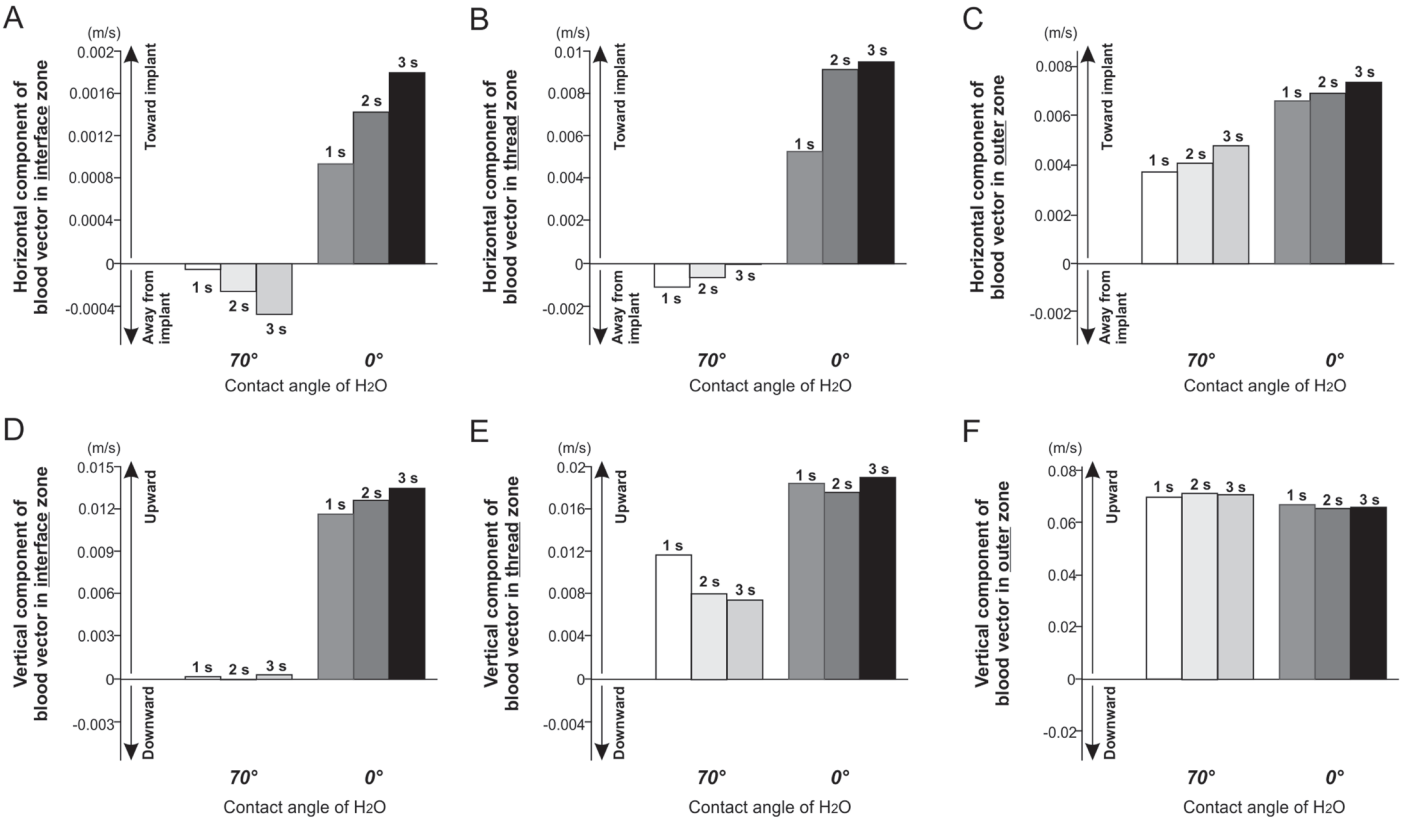

Fig. 4. Quantitative assessment of the direction and speed of whole blood flow. (A-C) Horizontal components of averaged vectors of the blood field. Histograms are shown for the interface, thread, and outer zones and presented to compare hydrophobic (70°) and superhydrophilic (0°) implants. (D-F) Vertical components of the averaged vectors of the blood field are shown.

3.5. Robust generation of vortices at the superhydrophilic interface

Next, by calculating the vorticity index from the vector information, we determined whether the whole blood dynamics included vortices (**Fig. 6**). The vorticity index was consistently high at the superhydrophilic interface and low with a time-dependent decline at the hydrophobic interface. The vortex flowed counterclockwise at the interface of both implants (**Fig. 6A**). Vortices were also counterclockwise in the thread zone and similar for both implants (**Fig. 6B**). Unlike in the interface and thread zones, the outer zone showed a clockwise vorticity index for both implants (**Fig. 6C**), which was more consistent and higher for the superhydrophilic implant. A comparison of vorticity indices in the three different zones revealed remarkably robust vortex formation at the superhydrophilic implant interface (**Figs. 6A-C**). The averaged vortex paths are illustrated in **Figure 5** (blue lines).

3.6. Vector visualization around hydrophobic and superhydrophilic implants

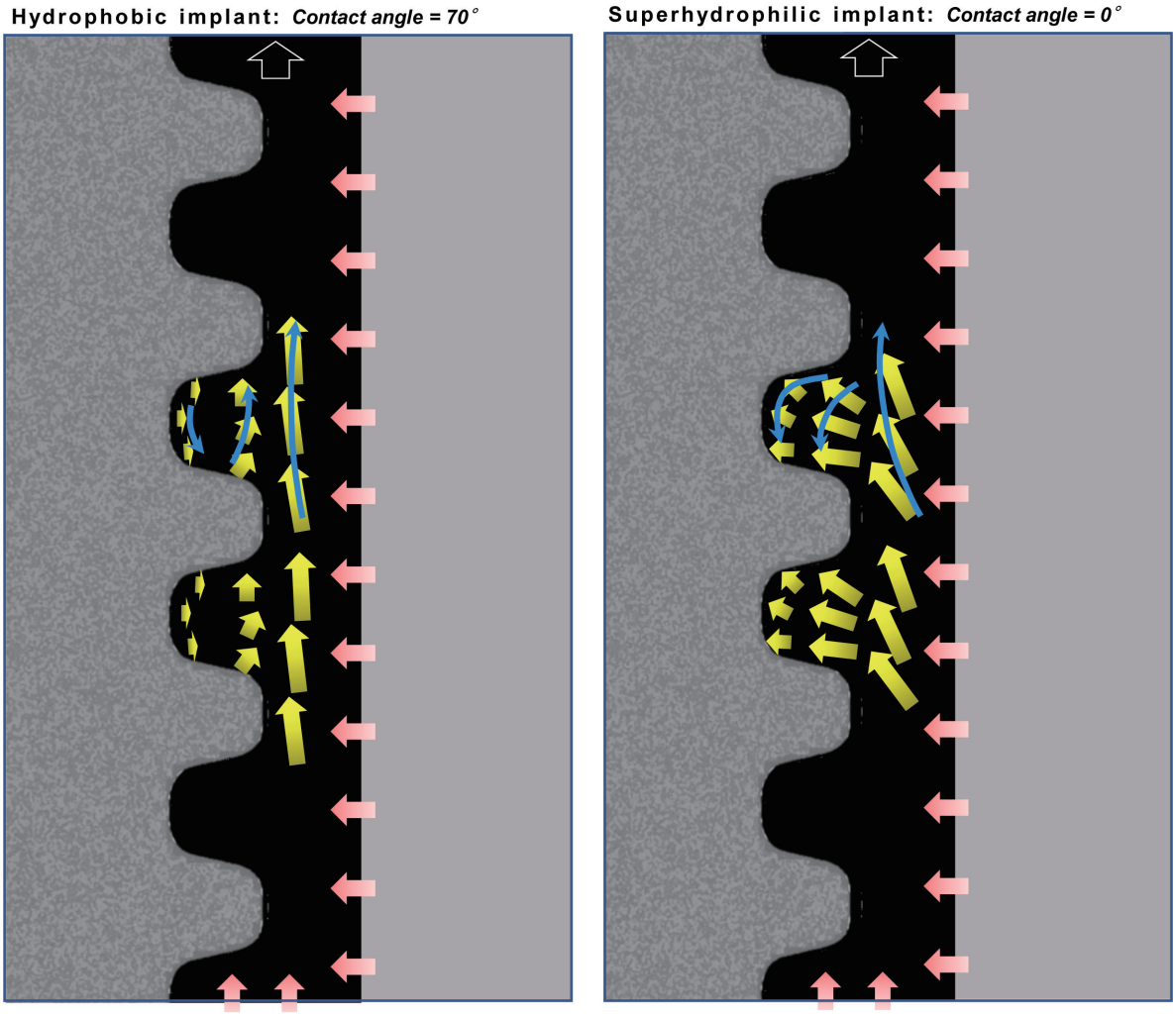

Fig. 5. Schematic of the whole blood flow (yellow arrows) based on the averaged vectors (**Fig. 4**), together with the whole blood streams (blue arrows) based on the average vorticity (**Fig. 6**)

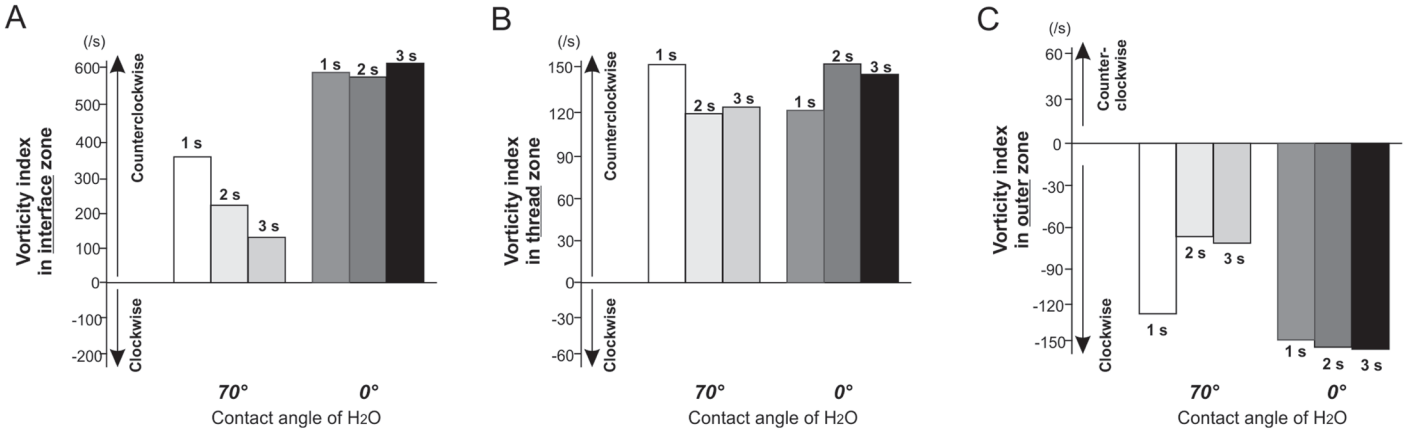

Fig. 6. Quantitative assessment of vortex formation during whole blood flow. (A-C) Vorticity index was calculated in each of the interface, thread, and outer zones and presented to compare hydrophobic (70°) and superhydrophilic (0°) implants. Note the different direction of vortex patterns indicated in the graphs.

We next color-mapped the individual vectors in the whole blood field (**Fig. 7**). Images in the transitional areas of the thread and outer zones revealed considerable differences between the two implants (**Figs. 7A and B**). Vectors around the hydrophobic implant

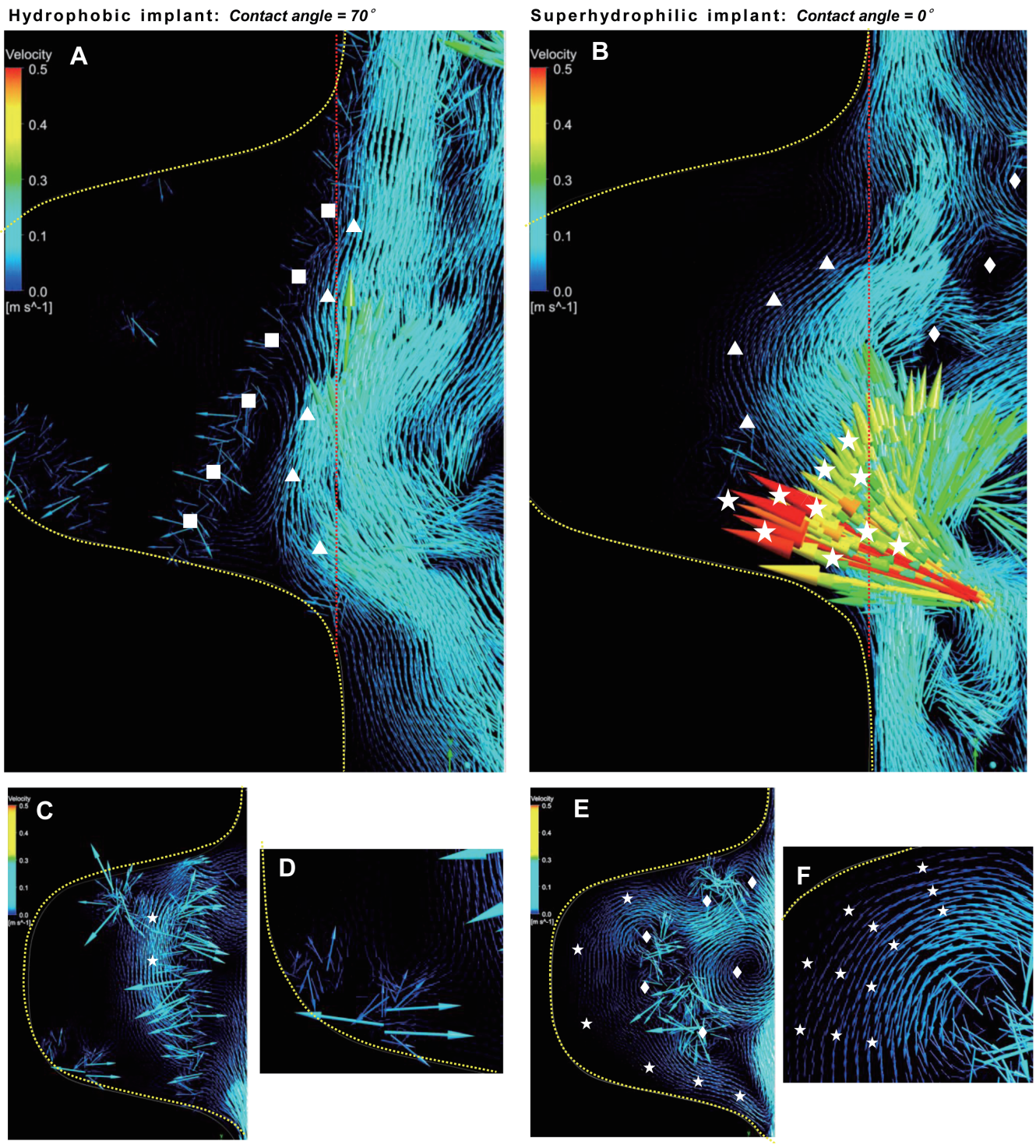

Fig. 7. Vector color-mapping during whole blood flow around hydrophobic and superhydrophilic implants. Each vector represents the direction and speed of the cell meshed in the domain, as defined in the color-coded scale. (A, B) Mapping images focusing on the transitional area between the outer and thread zones. (C-F) Focused images within the thread zone and at the implant interface. Refer to the main text for symbols.

were, in general, relatively mono-directional, with a slight angulation towards the implant in the lower half of the thread and away from the implant in the upper half of the thread. Vectors from the outer zone towards the thread zone seemed to be re-directed away from the implant, indicating that blood was pressured away without infiltrating into the thread zone (triangles in panel A). Around the hydrophobic implant only, a line created by outward and inward vectors across the entrance of the thread zone seemed to act as a critical barrier to repel blood influx (squares in panel A). As a result, only a small proportion of blood flux reached the thread zone by passing the red dotted line in panel A.

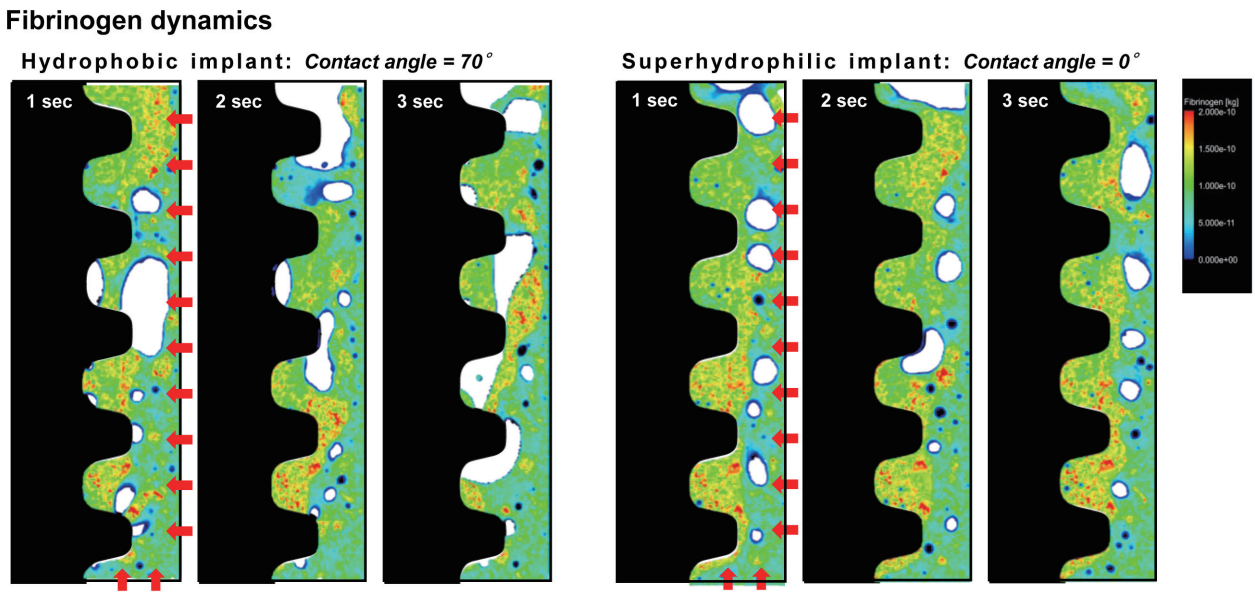

Fig. 8. Fibrinogen dynamics visualized by color mapping density and comparing the hydrophobic and superhydrophilic implants. Images from three different time points are presented. The blood inlet is indicated by red arrows.

In contrast, a considerable number of remarkably thick and long vectors were directed towards the thread zone around the superhydrophilic implant, as highlighted in red, yellow, and green and representing fast and massive whole blood influx (stars in panel B). Thus, significantly more vectors crossed the red line into the thread region. Similar to the re-directing pattern around the hydrophobic implant, some vectors returned to the outer zone, as outlined by triangles in panel B. This outflux created vortex nodes and repelling or attracting foci (diamonds in panel B).

In the thread (C) and interface (D) zones of the hydrophobic implant, the vectors were randomly directed. Although there was a weak stream of concentric, downward vectors in the middle of the thread zone (stars in panel C), the vectors in the interface zone were disordered and randomly located and did not form a stream (panels C and D), with a majority of vectors directed outward or away from the implant. The thread zone of the superhydrophilic implant was filled with multiple vortex nodes (diamonds in panel E) and formed mostly counterclockwise streams flowing close to the implant surface and along the implant outline (stars in panels E and F). These qualitative vector visualizations of whole blood were corroborated by the averaged vectors and vorticities illustrated in **Figure 5**.

3.7. Fibrinogen flow visualization around hydrophobic and superhydrophilic implants

We next examined the flow dynamics of fibrinogen, a representative wound-healing protein, by visualizing its density by color mapping (**Fig. 8**). Fibrinogen dynamics were similar to the blood plasma dynamics (**Fig. 2**), in that, although fibrinogen flowed into the thread zones of both implants, voids were found in the interface and thread zones of the hydrophobic implant throughout the analysis. The voids were large around the hydrophobic implant, and fibrinogen was densely located in the thread zone of the superhydrophilic implant but was scattered in the outer zone around the hydrophobic implant.

3.8. Quantitative assessment of fibrinogen dynamics

Based on the color mapping, we quantified the fibrinogen located in each zone of the two implants (**Fig. 9**). As shown in **Figure 9A**, fibrinogen density at the hydrophobic implant interface gradually increased over time, whereas it rapidly increased at the superhydrophilic interface and plateaued after only 0.5 seconds. Fibrinogen was approximately 20-times denser at the superhydrophilic interface than at the hydrophobic interface after 1 second of blood flow and remained 3-times denser even after 3 seconds. The fibrinogen concentration in the thread zone also rapidly increased around the superhydrophilic implant and remained high throughout the simulation period (**Fig. 9B**). In contrast, fibrinogen concentration peaked at 1.8 seconds for the hydrophobic implant and remained unchanged thereafter, indicating that it reached the steady state. The fibrinogen was 10- and 3.5-times denser for the superhydrophilic implant than for the hydrophobic implant at 1 and 3 seconds, respectively. Conversely, the fibrinogen density in the outer zone plateaued and reached the steady state immediately for both implants and was consistently lower for the superhydrophilic implant (**Fig. 9C**).

To determine if the distribution of fibrinogen was different in the three zones, we re-evaluated fibrinogen density relative to the total amount in the field. As shown in **Figure 9D**, compared with only 4.1% for the hydrophobic implant, 11.6% of total fibrinogen infiltrated the interface zone of the superhydrophilic implant by the end of analysis. Similarly, 38.0% of total fibrinogen flowed into the superhydrophilic thread zone but only 11% into the hydrophobic thread zone (**Fig. 9E**). Although only 50.4% fibrinogen remained in the outer zone of the superhydrophilic implant, 85% remained for the hydrophobic implant.

4. Discussion

In this study, we provide a comprehensive qualitative and quantitative analysis of blood and protein dynamics around metal-

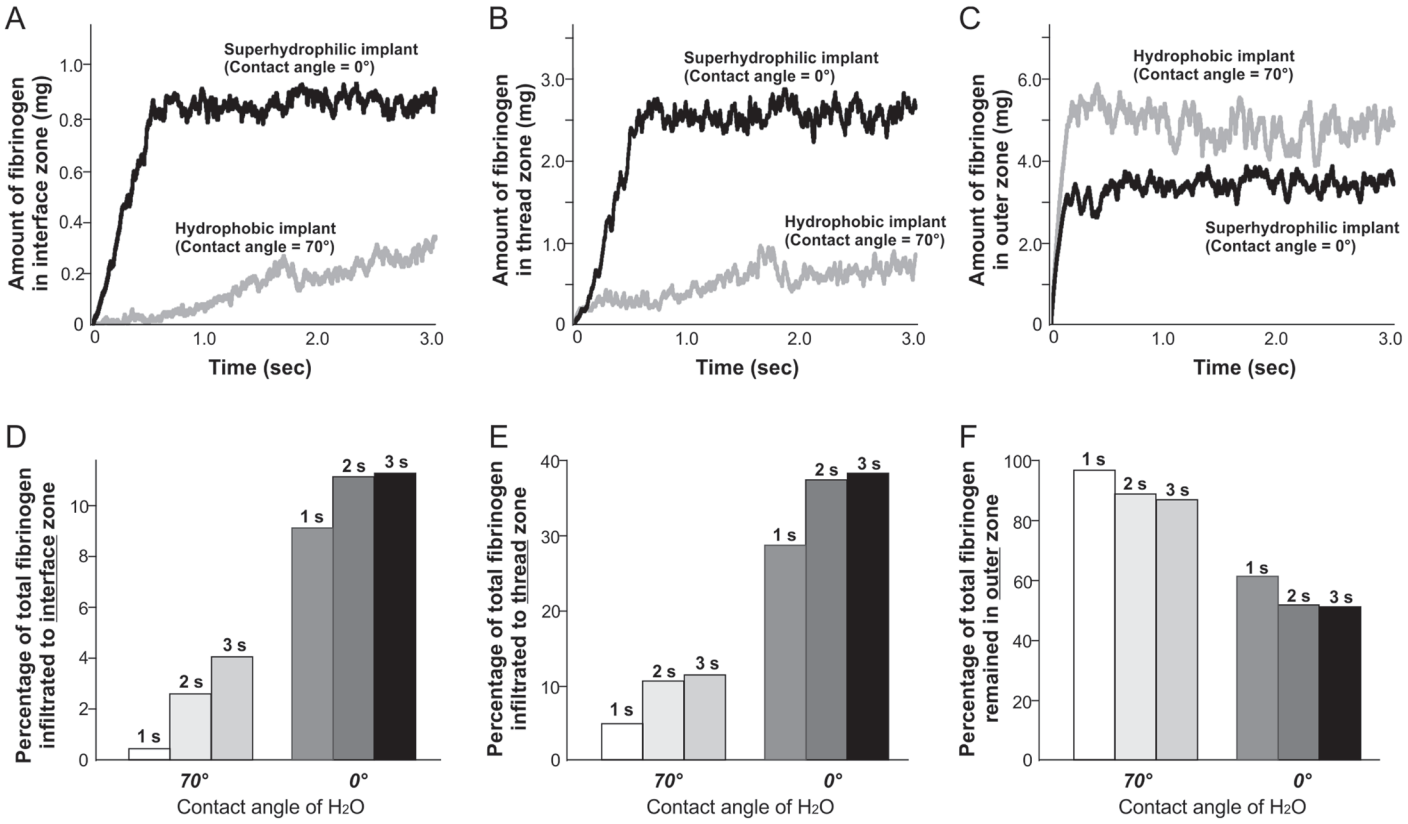

Fig. 9. Quantitative assessment of the localization and density of fibrinogen during blood flow. (A-C) The amount of fibrinogen changing with time in the interface, thread, and outer zones for hydrophobic and superhydrophilic implants. (D-F) Fibrinogen distribution in the different zones as indicated by the percentage of fibrinogen located in each zone relative to the total fibrinogen in the domain.

Table 1. Summary of blood dynamics regulated by hydrophobic and superhydrophilic implants

	Void			Vector			Streamline			Vortex		
	Interface	Thread	Outer	Interface	Thread	Outer	Interface	Thread	Outer	Interface	Thread	Outer
Hydrophobic implants	~45%	~40%	25%	Away	Away	Toward	None	Weak DW	Strong UW	Minor CC	Minor CC	Minor C
Superhydrophilic implants	Near 0	~5%	15%	Toward	Toward	Toward	Strong AI	Strong AI	Strong IF	Vigorous CC	Minor CC	Minor C

Away: Away from implant surface
Toward: Toward implant surface
DW: Downward
UW: Upward
AI: Along implant surface
IF: Influx
CC: Counter-clockwise
C: Clockwise

lic implants, and in doing so establish baseline knowledge on the processes underpinning bone-implant integration or osseointegration associated with macroscopic design and a physicochemical property. Specifically, we revealed that implant threads, regardless of hydrophobic or hydrophilic surfaces, significantly slow down blood flow along the long axis of the implants. A comparison of the effects of hydrophobicity and hydrophilicity on blood dynamics is provided in **Table 1**. Blood must influx the implant surface—or at least close to the implant surface—to deliver osteogenic and mesenchymal stem cells as well as the proteins necessary for bone-implant integration. However, we found that voids in blood plasma formed over 40% of the interface and thread zones of hydrophobic implants, which would be expected to significantly hinder delivery of these biological constituents (**Table 1**). More importantly, this phenomenon was nearly eliminated by superhydrophilicity (**Table 1**), which is a new discovery of the advantage of superhydrophilic implants. It was also notable that superhydrophilic surfaces reduced void formation in the outer zone (**Table 1**), indicating that the positive effect extends well beyond the area adjacent to the implant.

The lack of blood plasma was not the only drawback of hydrophobic implants. As shown by vector visualization of whole blood and quantitative analyses (**Figs. 4, 5, and 7; Table 1**), the blood flow within the threads of hydrophobic implants was unstable, dis-

Table 2. Summary of protein dynamics regulated by hydrophobic and superhydrophilic implants

	Influx speed			Influx quantity			Density		
	Interface	Thread	Outer	Interface	Thread	Outer	Interface	Thread	Outer
Hydrophobic implants	Slow TD	Slow TD	Rapid	~4%	~11%	~95%	0.00~0.48	0.15~0.36	1.56~1.40
Superhydrophilic implants	Rapid	Rapid	Rapid	~12%	~40%	~60%	1.03~1.32	0.92~1.28	0.97~0.80

TD: Time-dependent
Influx quantity: Expressed relative to total inlet
Density (D): Expressed in proportion among the zones. The distribution is even when D is 1.00, whereas protein is recruited more aggressively when D > 1.

ordered, and on average away from the implant surface compared with towards the implant surface for the superhydrophilic implant. The whole blood flow within the superhydrophilic thread was stable and generated multiple vortex nodes with blood streams consisting of ordered, concentric vectors along the implant surface curvature. These unique dynamics were supported by massive blood influx from the outer zone to the thread zone around the superhydrophilic implant. Conversely, there was a layer of conflicting vectors across the entrance to the thread zone of the hydrophobic implant, which seemed to act as a barrier to blood influx. The majority of whole blood flow from the outer zone of the hydrophobic implant appeared to be repelled at the entry of the thread zone before being forced upwards. It was noteworthy that blood plasma concentration was low at the void interface as represented by the blue lines in the color mapping (**Fig. 2**). This characteristic border was not seen at the implant interface. We believe that this is because of the influence of RBCs. The voids defined in this study are the lack of blood plasma and localization of RBCs. The co-presence of RBCs and blood plasma at the border of voids may have diluted the blood plasma concentration. We also noticed that the blood plasma local concentration was altered by the hydrophilic or hydrophobic state of implant surfaces. The interface and thread zones around the hydrophobic implant in the area adjacent to the blood inlet was low in blood plasma concentration despite the presence of plasma, which was significantly improved around the superhydrophilic implant (**Fig. 2**). This result was consistent from the beginning to the end of the time points analyzed. These results indicated that there may be disadvantageous areas in recruiting blood depending on where these areas are relative to the origin and direction of blood inlet, and more importantly, that superhydrophilic implants are capable of mitigating these disadvantages. Future studies using different thread designs and inlet conditions will help interpret these interesting results.

Fibrinogen flux was also influenced by the hydrophobicity or hydrophilicity of the implant surfaces, as summarized in **Table 2**. There was rapid fibrinogen influx into the thread and interface zones exclusively for the superhydrophilic implant (**Table 2 and Fig. 9**). Fibrinogen influx plateaued within 1 second for the superhydrophilic implant but only slowly and fractionally increased over time for the hydrophobic implant. There was an ~20-times difference in fibrinogen influx between the two implants. The smaller amount of fibrinogen left in the outer zone of the superhydrophilic implant confirmed that the superhydrophilic implant has the ability to recruit the protein (**Figs. 9C and F**). Based on the percentage of fibrinogen infiltrating into each zone relative to the total (**Figs. 9D-F**), we calculated the fibrinogen density (quantity/area) in each zone and expressed as a proportion among the three different zones (**Table 2**). First, the fibrinogen density was considerably lower in the interface (0.00–0.48 when the even distribution was 1.00) and thread (0.15–0.36) zones than in the outer zone of the hydrophobic implant (**Table 2**), meaning that the outer zone retained protein. Second, even for the hydrophobic implant, the fibrinogen density in the interface zone eventually exceeded that in the thread zone. Therefore, the majority of fibrinogen was located in the outer zone or at best was divided into the interface and outer zones, implying "distant" or "split" hemodynamics around the hydrophobic implant. In contrast, as shown in the density values (**Table 2**), fibrinogen was more concentrated in the interface and thread zones than in the outer zone for the superhydrophilic implant. Of particular note, the fibrinogen density was consistently higher in the interface zone than in the thread zone of the superhydrophilic implant. These results confirmed that superhydrophilic implants can better recruit protein close to the implant surface, which we term "contact hemodynamics." This newly defined hemodynamics is conceptualized and symbolically described in a graphic illustration (**Fig. 10)** and summarized in a short video (See the Results section 3.2.).

As noted above, peri-implant bone formation has distinct but unexplained behaviors. Regular titanium implants are hydrophobic, and a part of peri-implant bone forms circumferentially away from the implant (distant osteogenesis)[1,30]. This study shows that, specifically for the hydrophobic implant, a major blood mass flows nearly straight upwards outside of the implant threads without entering the threads. As a result, the cells and proteins necessary for bone formation, which are carried by this blood flow, may remain and inhabit this outer zone to provide a resource for satellite-like osteogenesis. Our new concept of split or distant hemodynamics may explain the distant osteogenesis occurring around regular titanium implants.

Our results, in particular the rapid and massive recruitment of blood into the interface zone without voids together with the uniquely aligned vectors toward the implant surface, help to explain the mechanism underlying enhanced bone-implant integration around superhydrophilic implant surfaces. Bone formation occurs contiguously at the superhydrophilic implant interface with almost no soft tissue intervention, in contrast to the fragmental bone formation around hydrophobic implant surfaces and 10–40% soft tissue intervention[30]. Fibrinogen density, which is influenced by the blood flow, was the highest at the superhydrophilic implant interface and the lowest in the outer zone, likely explaining why there is less bone formation in areas distant from superhydrophilic implant surfaces. The enhanced osteogenesis around superhydrophilic implants can be explained, at least partially, by the contact hemodynamics phenomenon.

It was important to design a CFD model carefully in this new field of implant studies. In implant research, the thread zone has always been a focus such that the area of bone formation has been evaluated within the threads. Considering the necessary, broad perspective of peri-implant osteogenesis, we included the surrounding area defined as an outer zone in the model, which

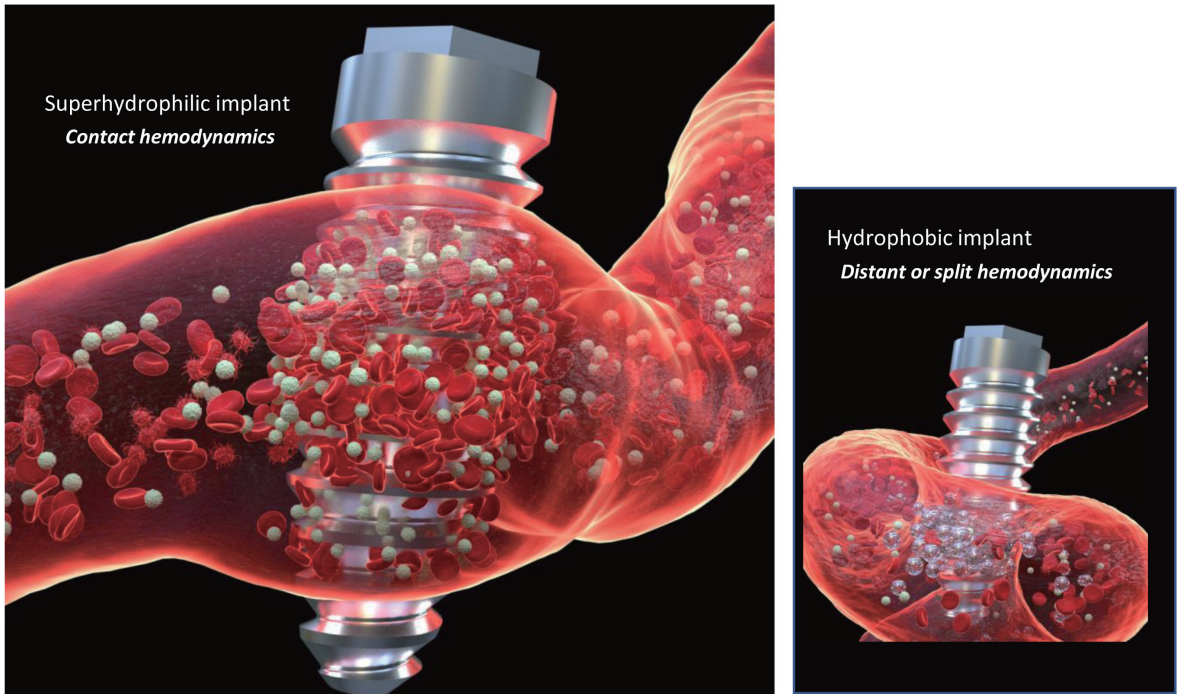

Fig. 10. Illustrative images representing the interaction between hydrophobic or superhydrophilic implants and blood, symbolizing a hemophobic implant (right) to induce distant hemodynamics or split hemodynamics and a superhemophilic implant (left) to enable contact hemodynamics. See the main text and **Tables 1 and 2** for a detailed description. This is a graphic illustration conceptualizing the results and and does not represent the CFD model used in this study.

presented results in contrast to those from the thread zone and justified the crucial assessments in both zones. In addition, we hypothesize that owing to the surface morphology, the blood flow may be influenced at the very interface of implants. The commonly used microrough surfaces, such as an acid-etch-created microrough surface, in dental implants have a roughness level of 2–5 μm in height[5,7,8,10,26,52,84–92]. When combined with sandblasting, the roughness increases to 5–15 μm[11,65,90–93]. Recent advancements in surface technology have enabled forming of meso-scale roughness with a microrough texture, whose roughness extends to up to 40 μm[4,21,22,94]. From the perspective of establishing a versatile CFD model applicable to various implant surfaces in the future, this study decided to define the interface zone as within the 40 μm vicinity. We validated the appearance of a hydrophilic surface on Grade 4 implants and titanium disks because the majority of implants are constructed from grade 4 titanium[90,93]. The effect of UV treatment, such as the conversion to a hydrophilic surface, has been demonstrated for various surface types and materials, including type 2 commercially pure titanium, grade 5 titanium alloy, and zirconia[29,31,38,41,42,46,47,49,50,55,63,64,66,69,72,95–97].

Blood and protein dynamics are therefore heavily influenced by implant morphology and material surface properties. This study provides a valuable mathematical model to test and optimize new implant designs. For instance, our model will allow the rapid and low-cost evaluation of different thread dimensions, angles, and textures that optimize blood and protein dynamics for osseointegration.

5. Conclusions

We visualized and quantified the flow and density of blood and fibrinogen using a CFD implant model. Screw-shaped implants were designed and hydrophobic and superhydrophilic surfaces compared. Blood plasma did not fill 40–50% of the implant interface or the inside of the threads around hydrophobic implants, whereas such voids were nearly eliminated around superhydrophilic implants. Whole blood field vectors were disorganized and directed randomly within hydrophobic threads but formed vortex nodes surrounded by concentric, stable blood streams along the superhydrophilic implant surface. The averaged vector within the thread was away from the implant surface for hydrophobic implants and towards the implant surface for the superhydrophilic implants. The fibrinogen density was up to 20-times greater at the superhydrophilic implant interface than at the hydrophobic interface. Furthermore, fibrinogen was intensively recruited to the superhydrophilic implant interface but distributed between the implant interface and the area outside the threads for the hydrophobic implant; the majority of fibrinogen was located in the outside area. This study evaluates, for the first time, the regulation of blood influx, vector and vortex formulation, and distribution of blood and proteins by implant threads and surface hydrophilicity. In doing so, the blood flow around hydrophobic and superhydrophilic implants can now be regarded as distant or split and contact hemodynamics, respectively.

Acknowledgements

This work was partially supported by DIO Implant.

Declaration of Competing Interest

There is no conflict of interest.

References

[1] Ogawa T, Nishimura I. Different bone integration profiles of turned and acid-etched implants associated with modulated expression of extracellular matrix genes. Int J Oral Maxillofac Implants. 2003;18:200–10. PMID:12705297

[2] Aita H, Att W, Ueno T, Yamada M, Hori N, Iwasa F, *et al.* Ultraviolet light-mediated photofunctionalization of titanium to promote human mesenchymal stem cell migration, attachment, proliferation and differentiation. Acta Biomater. 2009;5:3247–57. https://doi.org/10.1016/j.actbio.2009.04.022, PMID:19427421

[3] Ueno T, Yamada M, Suzuki T, Minamikawa H, Sato N, Hori N, *et al.* Enhancement of bone–titanium integration profile with UV-photofunctionalized titanium in a gap healing model. Biomaterials. 2010;31:1546–57. https://doi.org/10.1016/j.biomaterials.2009.11.018, PMID:19962757

[4] Hasegawa M, Saruta J, Hirota M, Taniyama T, Sugita Y, Kubo K, *et al.* A Newly Created Meso-, Micro-, and Nano-Scale Rough Titanium Surface Promotes Bone-Implant Integration. Int J Mol Sci. 2020;21:783. https://doi.org/10.3390/ijms21030783, PMID:31991761

[5] Kubo K, Att W, Yamada M, Ohmi K, Tsukimura N, Suzuki T, *et al.* Microtopography of titanium suppresses osteoblastic differentiation but enhances chondroblastic differentiation of rat femoral periosteum-derived cells. J Biomed Mater Res A. 2008;87A:380–91. https://doi.org/10.1002/jbm.a.31791, PMID:18181115

[6] Kubo K, Tsukimura N, Iwasa F, Ueno T, Saruwatari L, Aita H, *et al.* Cellular behavior on TiO2 nanonodular structures in a micro-to-nanoscale hierarchy model. Biomaterials. 2009;30:5319–29. https://doi.org/10.1016/j.biomaterials.2009.06.021, PMID:19589591

[7] Tsukimura N, Kojima N, Kubo K, Att W, Takeuchi K, Kameyama Y, *et al.* The effect of superficial chemistry of titanium on osteoblastic function. J Biomed Mater Res A. 2008;84A:108–16. https://doi.org/10.1002/jbm.a.31422, PMID:17600332

[8] Tsukimura N, Ueno T, Iwasa F, Minamikawa H, Sugita Y, Ishizaki K, *et al.* Bone integration capability of alkali- and heat-treated nanobimorphic Ti–15Mo–5Zr–3Al. Acta Biomater. 2011;7:4267–77. https://doi.org/10.1016/j.actbio.2011.08.016, PMID:21888994

[9] Tsukimura N, Yamada M, Iwasa F, Minamikawa H, Att W, Ueno T, *et al.* Synergistic effects of UV photofunctionalization and micro-nano hybrid topography on the biological properties of titanium. Biomaterials. 2011;32:4358–68. https://doi.org/10.1016/j.biomaterials.2011.03.001, PMID:21421270

[10] Ueno T, Tsukimura N, Yamada M, Ogawa T. Enhanced bone-integration capability of alkali- and heat-treated nanopolymorphic titanium in micro-to-nanoscale hierarchy. Biomaterials. 2011;32:7297–308. https://doi.org/10.1016/j.biomaterials.2011.06.033, PMID:21742375

[11] Ogawa T, Saruwatari L, Takeuchi K, Aita H, Ohno N. Ti nano-nodular structuring for bone integration and regeneration. J Dent Res. 2008;87:751–6. https://doi.org/10.1177/154405910808700809, PMID:18650547

[12] Nakamura HK, Butz F, Saruwatari L, Ogawa T. A role for proteoglycans in mineralized tissue-titanium adhesion. J Dent Res. 2007;86:147–52. https://doi.org/10.1177/154405910708600208, PMID:17251514

[13] Saruwatari L, Aita H, Butz F, Nakamura HK, Ouyang J, Yang Y, *et al.* Osteoblasts generate harder, stiffer, and more delamination-resistant mineralized tissue on titanium than on polystyrene, associated with distinct tissue micro- and ultrastructure. J Bone Miner Res. 2005;20:2002–16. https://doi.org/10.1359/JBMR.050703, PMID:16234974

[14] Takeuchi K, Saruwatari L, Nakamura HK, Yang JM, Ogawa T. Enhanced intrinsic biomechanical properties of osteoblastic mineralized tissue on roughened titanium surface. J Biomed Mater Res A. 2005;72A:296–305. https://doi.org/10.1002/jbm.a.30227, PMID:15654712

[15] Kligman S, Ren Z, Chung CH, Perillo MA, Chang YC, Koo H, *et al.* The Impact of Dental Implant Surface Modifications on Osseointegration and Biofilm Formation. J Clin Med. 2021;10:1641. https://doi.org/10.3390/jcm10081641, PMID:33921531

[16] Matos GRM. Surface Roughness of Dental Implant and Osseointegration. J Maxillofac Oral Surg. 2021;20:1–4. https://doi.org/10.1007/s12663-020-01437-5, PMID:33584035

[17] Ogle OE. Implant surface material, design, and osseointegration. Dent Clin North Am. 2015;59:505–20. https://doi.org/10.1016/j.cden.2014.12.003, PMID:25835806

[18] Souza JCM, Sordi MB, Kanazawa M, Ravindran S, Henriques B, Silva FS, *et al.* Nano-scale modification of titanium implant surfaces to enhance osseointegration. Acta Biomater. 2019;94:112–31. https://doi.org/10.1016/j.actbio.2019.05.045, PMID:31128320

[19] Albrektsson T, Wennerberg A. On osseointegration in relation to implant surfaces. Clin Implant Dent Relat Res. 2019;21(suppl 1):4–7. https://doi.org/10.1111/cid.12742, PMID:30816639

[20] Pellegrini G, Francetti L, Barbaro B, del Fabbro M. Novel surfaces and osseointegration in implant dentistry. J Investig Clin Dent. 2018;9:e12349. https://doi.org/10.1111/jicd.12349, PMID:29971928

[21] Rezaei NM, Hasegawa M, Ishijima M, Nakhaei K, Okubo T, Taniyama T, *et al.* Biological and osseointegration capabilities of hierarchically (meso-/micro-/nano-scale) roughened zirconia. Int J Nanomedicine. 2018;13:3381–95. https://doi.org/10.2147/IJN.S159955, PMID:29922058

[22] Saruta J, Ozawa R, Okubo T, Taleghani SR, Ishijima M, Kitajima H, *et al.* Biomimetic Zirconia with Cactus-Inspired Meso-Scale Spikes and Nano-Trabeculae for Enhanced Bone Integration. Int J Mol Sci. 2021;22:7969. https://doi.org/10.3390/ijms22157969, PMID:34360734

[23] Ogawa T, Nishimura I. Genes differentially expressed in titanium implant healing. J Dent Res. 2006;85:566–70. https://doi.org/10.1177/154405910608500617, PMID:16723657

[24] Ogawa T, Sukotjo C, Nishimura I. Modulated bone matrix-related gene expression is associated with differences in interfacial strength of different implant surface roughness. J Prosthodont. 2002;11:241–7. PMID:12501137

[25] Yamada M, Ueno T, Minamikawa H, Ikeda T, Nakagawa K, Ogawa T. Early-stage osseointegration capability of a submicrofeatured titanium surface created by microroughening and anodic oxidation. Clin Oral Implants Res. 2013;24:991–1001. PMID:22726210

[26] Yamada M, Ueno T, Tsukimura N, Ikeda T, Nakagawa K, Hori N, *et al.* Bone integration capability of nanopolymorphic crystalline hydroxyapatite coated on titanium implants. Int J Nanomedicine. 2012;7:859–73. PMID:22359461

[27] Funato A, Ogawa T. Photofunctionalized dental implants: a case series in compromised bone. Int J Oral Maxillofac Implants. 2013;28:1589–601. https://doi.org/10.11607/jomi.3232, PMID:24278928

[28] Funato A, Yamada M, Ogawa T. Success rate, healing time, and implant stability of photofunctionalized dental implants. Int J Oral Maxillofac Implants. 2013;28:1261–71. https://doi.org/10.11607/jomi.3263, PMID:24066316

[29] Att W, Takeuchi M, Suzuki T, Kubo K, Anpo M, Ogawa T. Enhanced osteoblast function on ultraviolet light-treated zirconia. Biomaterials. 2009;30:1273–80. https://doi.org/10.1016/j.biomaterials.2008.11.024, PMID:19095298

[30] Aita H, Hori N, Takeuchi M, Suzuki T, Yamada M, Anpo M, *et al.* The effect of ultraviolet functionalization of titanium on integration with bone. Biomaterials. 2009;30:1015–25. https://doi.org/10.1016/j.biomaterials.2008.11.004, PMID:19042016

[31] Hori N, Iwasa F, Tsukimura N, Sugita Y, Ueno T, Kojima N, *et al.* Effects of UV photofunctionalization on the nanotopography enhanced initial bioactivity of titanium. Acta Biomater. 2011;7:3679–91. https://doi.org/10.1016/j.actbio.2011.06.022, PMID:21723964

[32] Iwasa F, Hori N, Ueno T, Minamikawa H, Yamada M, Ogawa T. Enhancement of osteoblast adhesion to UV-photofunctionalized titanium via an electrostatic mechanism. Biomaterials. 2010;31:2717–27. https://doi.org/10.1016/j.biomaterials.2009.12.024, PMID:20035996

[33] Ueno T, Ikeda T, Tsukimura N, Ishijima M, Minamikawa H, Sugita Y, *et al.* Novel antioxidant capability of titanium induced by UV light treatment. Biomaterials. 2016;108:177–86. https://doi.org/10.1016/j.biomaterials.2016.08.050, PMID:27639113

[34] Ueno T, Yamada M, Hori N, Suzuki T, Ogawa T. Effect of ultraviolet photoactivation of titanium on osseointegration in a rat model. Int J Oral Maxillofac Implants. 2010;25:287–94. PMID:20369086

[35] Hirota M, Ozawa T, Iwai T, Mitsudo K, Ogawa T. UV-Mediated Photofunctionalization of Dental Implant: A Seven-Year Results of a Prospective Study. J Clin Med. 2020;9:2733. https://doi.org/10.3390/jcm9092733, PMID:32847061

[36] Hirota M, Ozawa T, Iwai T, Ogawa T, Tohnai I. Implant Stability Development of Photofunctionalized Implants Placed in Regular and Complex Cases: A Case-Control Study. Int J Oral Maxillofac Implants. 2016;31:676–86. https://doi.org/10.11607/jomi.4115, PMID:27183088

[37] Hirota M, Ozawa T, Iwai T, Ogawa T, Tohnai I. Effect of Photofunctionalization on Early Implant Failure. Int J Oral Maxillofac Implants. 2018;33:1098–102. https://doi.org/10.11607/jomi.6541, PMID:30231097

[38] Okubo T, Ikeda T, Saruta J, Tsukimura N, Hirota M, Ogawa T. Compromised Epithelial Cell Attachment after Polishing Titanium Surface and Its Restoration by UV Treatment. Materials (Basel). 2020;13:3946. https://doi.org/10.3390/ma13183946, PMID:32906598

[39] Okubo T, Tsukimura N, Taniyama T, Ishijima M, Nakhaei K, Rezaei NM, *et al.* Ultraviolet treatment restores bioactivity of titanium mesh plate degraded by contact with medical gloves. J Oral Sci. 2018;60:567–73. https://doi.org/10.2334/josnusd.17-0443, PMID:30587689

[40] Sugita Y, Honda Y, Kato I, Kubo K, Maeda H, Ogawa T. Role of photofunctionalization in mitigating impaired osseointegration associated with type 2 diabetes in rats. Int J Oral Maxillofac Implants. 2014;29:1293–300. https://doi.org/10.11607/jomi.3480, PMID:25397793

[41] Sugita Y, Saruta J, Taniyama T, Kitajima H, Hirota M, Ikeda T, *et al.* UV-Pre-Treated and Protein-Adsorbed Titanium Implants Exhibit Enhanced Osteoconductivity. Int J Mol Sci. 2020;21:4194. https://doi.org/10.3390/ijms21124194, PMID:32545509

[42] Iwasaki C, Hirota M, Tanaka M, Kitajima H, Tabuchi M, Ishijima M, *et al.* Tuning of Titanium Microfiber Scaffold with UV-Photofunctionalization for Enhanced Osteoblast Affinity and Function. Int J Mol Sci. 2020;21:738. https://doi.org/10.3390/ijms21030738, PMID:31979313

[43] Ghassemi A, Ishijima M, Hasegawa M, Mohammadzadeh Rezaei N, Nakhaei K, Sekiya T, *et al.* Biological and Physicochemical Characteristics of 2 Different Hydrophilic Surfaces Created by Saline-Storage and Ultraviolet Treatment. Implant Dent. 2018;27:405–14. https://doi.org/10.1097/ID.0000000000000773, PMID:29851661

[44] Taniyama T, Saruta J, Mohammadzadeh Rezaei N, Nakhaei K, Ghassemi A, Hirota M, *et al.* UV-Photofunctionalization of Titanium Promotes Mechanical Anchorage in A Rat Osteoporosis Model. Int J Mol Sci. 2020;21:1235. https://doi.org/10.3390/ijms21041235, PMID:32059603

[45] Ishijima M, Ghassemi A, Soltanzadeh P, Tanaka M, Nakhaei K, Park W, *et al.* Effect of UV Photofunctionalization on Osseointegration in Aged Rats. Implant Dent. 2016;25:744–50. https://doi.org/10.1097/ID.0000000000000459, PMID:27513161

[46] Ishijima M, Hirota M, Park W, Honda MJ, Tsukimura N, Isokawa K, *et al.* Osteogenic cell sheets reinforced with photofunctionalized micro-thin titanium. J Biomater Appl. 2015;29:1372–84. https://doi.org/10.1177/0885328214567693, PMID:25604095

[47] Ishijima M, Soltanzadeh P, Hirota M, Tsukimura N, Shigami T, Ogawa T. Enhancing osteoblast-affinity of titanium scaffolds for bone engineering by use of ultraviolet light treatment . Biomed Res. 2015;36:55–62. https://doi.org/10.2220/biomedres.36.55, PMID:25749151

[48] Iwasa F, Tsukimura N, Sugita Y, Kanuru RK, Kubo K, Hasnain H, *et al.* TiO2 micro-nano-hybrid surface to alleviate biological aging of UV-photofunctionalized titanium. Int J Nanomedicine. 2011;6:1327–41. PMID:21760728

[49] Tabuchi M, Hamajima K, Tanaka M, Sekiya T, Hirota M, Ogawa T. UV Light-Generated Superhydrophilicity of a Titanium Surface Enhances the Transfer, Diffusion and Adsorption of Osteogenic Factors from a Collagen Sponge. Int J Mol Sci. 2021;22:6811. https://doi.org/10.3390/ijms22136811, PMID:34202795

[50] Ikeda T, Okubo T, Saruta J, Hirota M, Kitajima H, Yanagisawa N, *et al.* Osteoblast Attachment Compromised by High and Low Temperature of Titanium and Its Restoration by UV Photofunctionalization. Materials (Basel). 2021;14:5493. https://doi.org/10.3390/ma14195493, PMID:34639891

[51] Att W, Hori N, Takeuchi M, Ouyang J, Yang Y, Anpo M, *et al.* Time-dependent degradation of titanium osteoconductivity: an implication of biological aging of implant materials. Biomaterials. 2009;30:5352–63. https://doi.org/10.1016/j.biomaterials.2009.06.040, PMID:19595450

[52] Ikeda T, Hagiwara Y, Hirota M, Tabuchi M, Yamada M, Sugita Y, *et al.* Effect of photofunctionalization on fluoride-treated nanofeatured titanium. J Biomater Appl. 2014;28:1200–12. https://doi.org/10.1177/0885328213501566, PMID:23985537

[53] Hirota M, Ikeda T, Sugita Y, Ishijima M, Hirota S, Ogawa T. Impaired osteoblastic behavior and function on saliva-contaminated titanium and its restoration by UV treatment. Mater Sci Eng C. 2019;100:165–77. https://doi.org/10.1016/j.msec.2019.03.008, PMID:30948050

[54] Hirota M, Ikeda T, Tabuchi M, Iwai T, Tohnai I, Ogawa T. Effect of ultraviolet-mediated photofunctionalization for bone formation around medical titanium mesh. J Oral Maxillofac Surg. 2014;72:1691–702. https://doi.org/10.1016/j.joms.2014.05.012, PMID:25109583

[55] Hirota M, Ikeda T, Tabuchi M, Nakagawa K, Park W, Ishijima M, *et al.* Bone Generation Profiling Around Photofunctionalized Titanium Mesh. Int J Oral Maxillofac Implants. 2016;31:73–86. https://doi.org/10.11607/jomi.4036, PMID:26800164

[56] Hori N, Att W, Ueno T, Sato N, Yamada M, Saruwatari L, *et al.* Age-dependent degradation of the protein adsorption capacity of titanium. J Dent Res. 2009;88:663–7. https://doi.org/10.1177/0022034509339567, PMID:19641155

[57] Hori N, Ueno T, Minamikawa H, Iwasa F, Yoshino F, Kimoto K, *et al.* Electrostatic control of protein adsorption on UV-photofunctionalized titanium. Acta Biomater. 2010;6:4175–80. https://doi.org/10.1016/j.actbio.2010.05.006, PMID:20466081

[58] Lee JH, Ogawa T. The biological aging of titanium implants. Implant Dent. 2012;21:415–21. https://doi.org/10.1097/ID.0b013e31826a51f4, PMID:22968574

[59] Ogawa T. Ultraviolet photofunctionalization of titanium implants. Int J Oral Maxillofac Implants. 2014;29:e95–102. https://doi.org/10.11607/jomi.te47, PMID:24451893

[60] Suzuki T, Kubo K, Hori N, Yamada M, Kojima N, Sugita Y, *et al.* Nonvolatile buffer coating of titanium to prevent its biological aging and for drug delivery. Biomaterials. 2010;31:4818–28. https://doi.org/10.1016/j.biomaterials.2010.02.061, PMID:20350765

[61] Gittens RA, Scheideler L, Rupp F, Hyzy SL, Geis-Gerstorfer J, Schwartz Z, *et al.* A review on the wettability of dental implant surfaces II: biological and clinical aspects. Acta Biomater. 2014;10:2907–18. https://doi.org/10.1016/j.actbio.2014.03.032, PMID:24709541

[62] Rupp F, Gittens RA, Scheideler L, Marmur A, Boyan BD, Schwartz Z, *et al.* A review on the wettability of dental implant surfaces I: theoretical and experimental aspects. Acta Biomater. 2014;10:2894–906. https://doi.org/10.1016/j.actbio.2014.02.040, PMID:24590162

[63] Hirota M, Sugita Y, Ishijima M, Ikeda T, Saruta J, Maeda H, *et al.* UV photocatalytic activity of titanium dioxide (TiO2) surface contaminated with bacterial biofilm: Implications for photo- restoration of osteoconductivity. Materials Today Advances 2021.

[64] Att W, Hori N, Iwasa F, Yamada M, Ueno T, Ogawa T. The effect of UV-photofunctionalization on the time-related bioactivity of titanium and chromium–cobalt alloys. Biomaterials. 2009;30:4268–76. https://doi.org/10.1016/j.biomaterials.2009.04.048, PMID:19473697

[65] Minamikawa H, Ikeda T, Att W, Hagiwara Y, Hirota M, Tabuchi M, *et al.* Photofunctionalization increases the bioactivity and osteoconductivity of the titanium alloy Ti6Al4V. J Biomed Mater Res A. 2014;102:3618–30. https://doi.org/10.1002/jbm.a.35030, PMID:24248891

[66] Tabuchi M, Ikeda T, Hirota M, Nakagawa K, Park W, Miyazawa K, *et al.* Effect of UV Photofunctionalization on Biologic and Anchoring Capability of Orthodontic Miniscrews. Int J Oral Maxillofac Implants. 2015;30:868–79. https://doi.org/10.11607/jomi.3994, PMID:26252039

[67] Tabuchi M, Ikeda T, Nakagawa K, Hirota M, Park W, Miyazawa K, *et al.* Ultraviolet photofunctionalization increases removal torque values and horizontal stability of orthodontic miniscrews. Am J Orthod Dentofacial Orthop. 2015;148:274–82. https://doi.org/10.1016/j.ajodo.2015.03.022, PMID:26232836

[68] Hirota M, Tanaka M, Ishijima M, Iwasaki C, Park W, Ogawa T. Effect of Photofunctionalization on Ti6Al4V Screw Stability Placed in Segmental Bone Defects in Rat Femurs. J Oral Maxillofac Surg. 2016;74:861. https://doi.org/10.1016/j.ajodo.2015.03.022

[69] Yamada M, Miyauchi T, Yamamoto A, Iwasa F, Takeuchi M, Anpo M, *et al.* Enhancement of adhesion strength and cellular stiffness of osteoblasts on mirror-polished titanium surface by UV-photofunctionalization. Acta Biomater. 2010;6:4578–88. https://doi.org/10.1016/j.actbio.2010.07.010, PMID:20633705

[70] Hori N, Ueno T, Suzuki T, Yamada M, Att W, Okada S, *et al.* Ultraviolet light treatment for the restoration of age-related degradation of titanium bioactivity. Int J Oral Maxillofac Implants. 2010;25:49–62. PMID:20209187

[71] Miyauchi T, Yamada M, Yamamoto A, Iwasa F, Suzawa T, Kamijo R, *et al.* The enhanced characteristics of osteoblast adhesion to photofunctionalized nanoscale TiO2 layers on biomaterials surfaces. Biomaterials. 2010;31:3827–39. https://doi.org/10.1016/j.biomaterials.2010.01.133, PMID:20153521

[72] Saita M, Ikeda T, Yamada M, Kimoto K, Lee MC, Ogawa T. UV photofunctionalization promotes nano-biomimetic apatite deposition on titanium. Int J Nanomedicine. 2016;11:223–34. PMID:26834469

[73] Att W, Ogawa T. Biological aging of implant surfaces and their restoration with ultraviolet light treatment: a novel understanding of osseointegration. Int J Oral Maxillofac Implants. 2012;27:753–61. PMID:22848875

[74] ANSYS I. Ansys Fluent Theory Guide. 2022, p. 224.

[75] ANSYS I. Ansys Fluent User's Guide. 2022, p. 1587.

[76] Mottaghy K, Hahn A. Interfacial tension of some biological fluids: a comparative study. Clin Chem Lab Med. 1981;19:267–72. https://doi.org/10.1515/cclm.1981.19.5.267, PMID:7264568

[77] Nauman JV, Campbell PG, Lanni F, Anderson JL. Diffusion of insulin-like growth factor-I and ribonuclease through fibrin gels. Biophys J. 2007;92:4444–50. https://doi.org/10.1529/biophysj.106.102699, PMID:17400703

[78] Density of blood. The Physics Factbook https://hypertextbook.com/facts/2004/MichaelShmukler.shtml

[79] Lanotte L, Mauer J, Mendez S, Fedosov DA, Fromental JM, Claveria V, *et al.* Red cells' dynamic morphologies govern blood shear thinning under microcirculatory flow conditions. Proc Natl Acad Sci USA. 2016;113:13289–94. https://doi.org/10.1073/pnas.1608074113, PMID:27834220

[80] Wufsus AR, Macera NE, Neeves KB. The hydraulic permeability of blood clots as a function of fibrin and platelet density. Biophys J. 2013;104:1812–23. https://doi.org/10.1016/j.bpj.2013.02.055, PMID:23601328

[81] Kitajima H, Hirota M, Iwai T, Hamajima K, Ozawa R, Hayashi Y, *et al.* Computational Fluid Simulation of Fibrinogen around Dental Implant Surfaces. Int J Mol Sci. 2020;21:660. https://doi.org/10.3390/ijms21020660, PMID:31963895

[82] Gurov I, Volkov M, Margaryants N, Pimenov A, Potemkin A. High-speed video capillaroscopy method for imaging and evaluation of moving red blood cells. Opt Lasers Eng. 2018;104:244–51. https://doi.org/10.1016/j.optlaseng.2017.09.003

[83] Sniegoski LT, Moody JR. Determination of serum and blood densities. Anal Chem. 1979;51:1577–8. https://doi.org/10.1021/ac50045a052, PMID:484867

[84] Ogawa T, Ozawa S, Shih JH, Ryu KH, Sukotjo C, Yang JM, *et al.* Biomechanical evaluation of osseous implants having different surface topographies in rats. J Dent Res. 2000;79:1857–63. https://doi.org/10.1177/002203450007901 10701, PMID:11145355

[85] Saruta J, Sato N, Ishijima M, Okubo T, Hirota M, Ogawa T. Disproportionate Effect of Sub-Micron Topography on Osteoconductive Capability of Titanium. Int J Mol Sci. 2019;20:4027. https://doi.org/10.3390/ijms20164027, PMID:31426563

[86] Nakamura H, Saruwatari L, Aita H, Takeuchi K, Ogawa T. Molecular and biomechanical characterization of mineralized tissue by dental pulp cells on titanium. J Dent Res. 2005;84:515–20. https://doi.org/10.1177/154405910508400606, PMID:15914587

[87] Att W, Tsukimura N, Suzuki T, Ogawa T. Effect of supramicron roughness characteristics produced by 1- and 2-step acid etching on the osseointegration capability of titanium. Int J Oral Maxillofac Implants. 2007;22:719–28. PMID:17974105

[88] Att W, Yamada M, Ogawa T. Effect of titanium surface characteristics on the behavior and function of oral fibroblasts. Int J Oral Maxillofac Implants. 2009;24:419–31. PMID:19587863

[89] Sato N, Kubo K, Yamada M, Hori N, Suzuki T, Maeda H, *et al.* Osteoblast mechanoresponses on Ti with different surface topographies. J Dent Res. 2009;88:812–6. https://doi.org/10.1177/0022034509343101, PMID:19767577

[90] Dohan Ehrenfest DM, Corso MD, Kang BS, Leclercq P, Mazor Z, Horowitz RA, *et al.* Identification card and codification of the chemical and morphological characteristics of 62 dental implant surfaces. Part 3: sand-blasted/acid-etched (SLA type) and related surfaces (Group 2A, main subtractive process). POSEIDO. 2014;2:37–55.

[91] Uno M, Hayashi M, Ozawa R, Saruta J, Ishigami H, Ogawa T. Mechanical Interlocking Capacity of Titanium with Respect to Surface Morphology and Topographical Parameters. J Dent Oral Biol. 2020;5:1163.

[92] Uno M, Ozawa R, Hamajima K, Saruta J, Ishigami H, Ogawa T. Variation in Osteoblast Retention Ability of Titanium Surfaces with Different Topographies. J Dent Oral Biol. 2020;5:1169.

[93] Dohan Ehrenfest DM, Vazquez L, Park YJ, Sammartino G, Bernard JP. Identification card and codification of the chemical and morphological characteristics of 14 dental implant surfaces. J Oral Implantol. 2011;37:525–42. https://doi.org/10.1563/AAID-JOI-D-11-00080, PMID:21728785

[94] Kitajima H, Komatsu K, Matsuura T, Ozawa R, Saruta J, Taleghani SR, *et al.* Impact of nano-scale trabecula size on osteoblastic behavior and function in a meso-nano hybrid rough biomimetic zirconia model. J Prosthodont Res; Online ahead of print. https://doi.org/10.2186/jpr.JPR_D_22_00015, PMID:35858802

[95] Park W, Ishijima M, Hirota M, Soltanzadeh P, Ogawa T. Engineering bone-implant integration with photofunctionalized titanium microfibers. J Biomater Appl. 2016;30:1242–50. https://doi.org/10.1177/0885328215620034, PMID:26656313

[96] Tateshima S, Kaneko N, Yamada M, Duckwiler G, Vinuela F, Ogawa T. Increased affinity of endothelial cells to NiTi using ultraviolet irradiation: An *in vitro* study. J Biomed Mater Res A. 2018;106:1034–8. https://doi.org/10.1002/jbm.a.36304, PMID:29218785

[97] Ishijima M, de Avila E, Nakhaei K, Shi W, Lux R, Ogawa T. Ultraviolet Light Treatment of Titanium Suppresses Human Oral Bacterial Attachment and Biofilm Formation: A Short-Term In Vitro Study. Int J Oral Maxillofac Implants. 2019;34:1105–13. https://doi.org/10.11607/jomi.7444, PMID:30807627